Oceanography Magazine Submission

Internal gravity wave modeling on basin to global scales and its impacts on acoustic propagation

Martha C. Schönau[1*,7], Luna Hiron[2], John Ragland[3,10], Keshav J. Raja[2], Joseph Skitka[4,8], Miguel S. Solano[5,9], Xiaobiao Xu[2], Brian K. Arbic[4], Maarten C. Buijsman[5], Eric P. Chassignet[2], Emanuel Coelho[1], Robert W. Helber[6], William Peria[3], Jay F. Shriver[6], Jason E. Summers[3], Kathryn L. Verlinden[1], Alan J. Wallcraft[2]

[1]Applied Ocean Sciences (AOS), LLC

[2]Center for Ocean-Atmospheric Prediction Studies, Florida State University

[3]Applied Research in Acoustics LLC (ARiA)

[4]Department of Earth and Environmental Sciences, University of Michigan

[5]School of Ocean Science and Engineering, The University of Southern Mississippi

[6]Naval Research Laboratory, Ocean Dynamics and Prediction

[7]Scripps Institution of Oceanography, University of California, San Diego

[8]Department of Physical Oceanography, Woods Hole Oceanographic Institution

[9]SOFAR Ocean Technologies

[10]Department of Electrical and Computer Engineering, University of Washington

[*]Corresponding author: mschonau@ucsd.edu.

Abstract:

Underwater acoustic propagation depends on ocean temperature, salinity, pressure, and bathymetry. The realistic representation of the ocean state and its underlying dynamics within ocean models is essential to accurately model and predict underwater acoustic propagation.

Stratified, high-resolution global ocean models that include tidal forcing have only been developed in the last two decades. Tidal forcing introduces internal tides and generates higher frequency (supertidal) internal waves. The inclusion of tides in global ocean models better captures the ocean state. Through the disciplines of internal wave modeling, acoustics and machine learning, we examined the movement of internal wave energy through numerical simulations, how the inclusion of tides in the models may impact acoustic propagation, and how machine learning may be used to simplify the modeling of these impacts. The project used global, basin-scale, and idealized HYbrid Coordinate Ocean Model (HYCOM) simulations as well as regional Massachusetts Institute of Technology general circulation model (MITgcm) simulations to examine the impacts of tidal inclusion on sea surface height variability, the propagation and dissipation of internal-wave energy, and the sensitivity of internal wave modeling to vertical and horizontal grid spacing. Sound speed, acoustic parameters, and acoustic propagation were compared between simulations both with and without tidal forcing. Deep learning algorithms were used to replicate some of the ocean structure variability at test locations through generation of a "tidal" simulation output from global HYCOM without tidal forcing. The cross-disciplinary effort between ocean modeling and acoustic assessment elucidated the impacts of certain ocean modeling choices (e.g., vertical and horizontal grid spacing, the hydrostatic assumption, and others) on sound speed and explored methods to reduce computational costs.

1. Introduction

Global ocean models are used by many stakeholders who are interested in (among others) how the ocean state (e.g., velocities, temperature, and salinity) may impact navigation, climate, the dispersal of biogeochemical tracers, biological productivity, and acoustic propagation, such as passive acoustic soundscape monitoring and acoustic communications between vessels or marine mammals. The propagation of acoustic waves (sound) in the ocean depends on the thermohaline structure of the ocean—the temperature, salinity, and pressure—and the bathymetry (shape of the seafloor). Sound refraction is caused by changes in temperature and salinity structure that impact density (relative pressure) and its gradients, such as fronts, eddies, currents, vertical stratification, and mixing. Processes that impact the thermohaline structure include energy input from wind, salinity changes at the ocean surface from evaporation and precipitation, surface temperature evolution from ocean-atmosphere heat exchange, and spatial and temporal variability of large-scale ocean currents that then spawn mesoscale eddies (with horizontal scales of about 100 km). A tidally forced ocean model, which simulates energy that can propagate then as internal tides and waves, will create sound-speed structure that may be very different from that of a non-tidally forced ocean model.

This paper presents new advancements in the modeling of internal tides and gravity waves and their impact on the propagation of acoustic waves. Internal gravity waves (IGWs) are waves with a restoring force of gravity, that exist as undulations along constant density ocean layers called isopycnal surfaces. IGWs create a profile of depth-dependent velocities, alongside the displacement of isopycnals. They are often discussed in terms of their vertical structure, or "modes" (Gill, 1982), which decomposes internal tides and waves to study the dynamics of IGW interactions and energy transfer. In this method, oceanic IGWs can be approximated as a linear superposition of standing waves in the vertical direction and propagating waves in the horizontal direction, which is a reasonable approximation in buoyancy driven flows where the horizontal scale of the flow is much greater than that in the vertical. Each wave mode has a characteristic length and phase speed (eigenvalue) and vertical structure (eigenfunction) that depends on the frequency of the IGW, the Coriolis frequency (arising from the projection of Earth's rotation), and vertical stratification (i.e., vertical density gradient or buoyancy frequency). The lowest-baroclinic mode has a singular, two-layer horizontal structure (i.e., the velocities are out of phase above and below the thermocline), and higher modes have greater vertical structure.

Internal tides are a special case of internal gravity waves that exist at tidal frequencies and are generated by tidal flow over bathymetric features of the seafloor (e.g., Bell, 1975; Arbic et al., 2004; Buijsman et al, 2020). Such flows create vertical motions, including vertical displacements along isopycnal surfaces. These are different from IGWs generated by high-frequency wind forcing, which causes near-inertial IGWs with a frequency that is near the Coriolis frequency (Pollard and Millard, 1970; Alford, 2003; Simmons and Alford, 2012, Raja et al., 2022). As the Coriolis frequency increases towards the poles, near-inertial IGW oscillation frequency also depends on latitude. Aside from internal tides and near-inertial waves, there exists an internal gravity wave continuum spectrum (Garrett and Munk, 1975). The high-frequency waves in the IGW continuum spectrum have supertidal frequencies (frequencies greater than tidal frequencies) and are thought to arise from nonlinear interactions between internal tides and near-inertial waves (Olbers, 1976; McComas and Bretherton, 1977; Müller et al., 1986).

Mesoscale eddies may also play a role in the formation of the spectrum (Barkan et al., 2017; Skitka et al., 2024; Delpech et al., 2024). These nonlinear interactions can change the length and time scales of IGWs, and we saw some evidence of them in this study.

IGW variability has not been well-captured by global ocean simulations, which may have incomplete forcing (e.g., a lack of tidal forcing) or may parameterize, rather than resolve, processes that happen at finer scales because the model horizontal and/or vertical discretization is too coarse. Models of the large-scale barotropic tides (where there is uniform water movement with depth) are often performed in a one-layer ocean of constant-density, that does not allow for any flow fields with vertical structure or undulations of density surfaces. Barotropic tidal models have been available since the 1970s (e.g., Hendershott, 1981). However, only in the last two decades has the increase in computational power allowed accurate modeling of internal tides in a stratified ocean. These have evolved from using uniform two-layer (Arbic et al., 2004) or multilayer (Niwa and Hibiya, 2004; Simmons et al., 2004) stratification in the horizontal direction to the inclusion of realistic horizontally varying stratification by embedding tidal forcing in ocean general circulation simulations (Arbic et al., 2010, 2012, 2018; Shriver et al., 2012; Buijsman et al., 2020; Arbic, 2022).

These models feature high-frequency undulations of density surfaces, including internal tides and supertidal IGWs, that bring cold water up and push warm water down, and therefore change the sound speed (Gill, 1982). The nonlinear interactions in the IGW continuum spectrum eventually bring internal wave scales down to the order of 1 m or less, at which IGWs turn over and break. Breaking IGWs play a dominant role in the mixing of the interior ocean, that is, the ocean away from coastal boundaries, the air-sea interface, and the bottom boundary at the seafloor (e.g., Munk and Wunsch, 1998; Alford, 2001; Waterhouse et al., 2014, MacKinnon et al., 2017). The impacts on acoustic propagation will also likely be influenced by model grid spacing, boundary conditions and parameterizations, as these all impact the IGW structure.

Internal waves and tides can cause significant impacts on sound speed variability and acoustic propagation (Flatté et al., 1979, Colosi et al. 2013). Acoustic tomography, an inverse method that uses long-range acoustic propagations to extrapolate the ocean structure, has been used to study the barotropic and baroclinic tides (e.g., Dushaw et al., 1995; Dushaw et al., 2011), and shown as a way to constrain ocean models themselves (Dushaw, 2019; Dushaw and Menemenlis, 2023). There have been many acoustical observational studies in strong tidal regions (e.g., Worcester et al., 2013) and efforts have been made to model these impacts using both acoustic arrival times and acoustic mode amplitudes (Colosi and Flatté, 1996; Chandrayadula et al., 2020). The advances in global models to include tidal forcing at high resolutions provides an opportunity to address how acoustic propagation may responds to the ocean model forcing and grid discretization.

This coordinated research project focuses on the modeling of IGWs and the impacts of IGWs on underwater acoustic propagation. The project was funded under the Task Force Ocean (TFO) Office of Naval Research (ONR) research initiative, and dubbed “TFO-HYCOM”, after the U.S. Navy’s operational HYbrid Coordinate Ocean Model (HYCOM). This article describes our progress in global internal wave modeling, our approach to assess the impacts that the modeling choices may have on mid-range, upper-ocean acoustics, and a preliminary exploration of how deep learning (DL) may be used to optimize the predictions of these impacts.

2. Internal wave modeling and their impacts on sound speed

The inclusion of tidal forcing in ocean models brings simulations closer to observations (e.g., Müller et al. 2015), which is a central effort in ocean modeling. This is illustrated by comparing high-resolution regional North Atlantic HYCOM simulations with tides and high-resolution bathymetry to satellite observations (Figure 1). HYCOM is the backbone of the operational forecasting system of the U.S. Navy (Chassignet et al., 2003, 2009; Metzger et al., 2014). The Navy HYCOM simulations use a hybrid vertical-coordinate system: isopycnal coordinates in the stratified ocean interior, and a dynamically transition to depth (z) coordinates in the surface mixed layer and to terrain-following (σ) coordinates (which follow the bathymetry) in shallow shelf water. The simulations use realistic atmospheric forcing from the Navy Global Environmental Model (NAVGEM) (Hogan et al., 2014), and can be run with or without data assimilation and with or without tidal forcing. Sophisticated methods from the data-assimilation literature have also been applied to bring the tidal simulations closer to observations (Ngodock et al., 2016). The HYCOM model was used in this study with a variety of vertical and horizontal grid-spacing and conditions.

Sea-surface height (SSH), available from satellite altimetry, is a useful proxy for mesoscale oceanic variability. The SSH wavenumber spectral slope is a measure of the relative strength of oceanic flows as a function of length-scales within a given domain. Wavenumber is defined as 2π or one divided by wavelength, hence large wavenumbers are associated with smaller spatial scales. For example, the wavelength of the first mode of the internal tide on the Amazon Shelf is around ~120 km and that of the second mode ~ 70 km (Xu et al., 2022). However, wavenumber spectral slopes vary greatly by location (Figure 1a, Xu and Fu, 2012; Zhou et al., 2015; Dufau et al., 2016), with steep spectral slopes in western boundary current regimes such as the Gulf Stream (which has strong currents and high eddy variability), flatter slopes in the interior (such as the eastern North Atlantic), and much flatter slopes in the equatorial region (Figure 4a). However, previously published results in high-resolution models without tidal forcing could not replicate this spatial variability (e.g., Figures 1e-f; Chassignet and Xu, 2017). Motivated by this apparent discrepancy, Xu et al. (2022) investigated the relative impacts of the inclusion of tidal forcing, high-resolution bathymetry, and high-frequency atmospheric forcing on the SSH wavenumber spectra using a series of 1/50° North and equatorial Atlantic HYCOM simulations. At this resolution, the models can realistically capture variability at scales of 10's to 100's of kilometers and both the barotropic and baroclinic tides. The inclusion of internal tides was paramount to improving the agreement with observations (Figures 1b-d). The surface signature of internal tides was greatest in the equatorial Atlantic and the eastern subtropical North Atlantic where there are strong barotropic tides and a strong stratification in the upper layer of the water column. The internal tides are the primary cause of the observed large spatial variability of the spectral slope in the Atlantic. High-resolution bathymetry and high-frequency wind variability had comparably minor impacts on the SSH variability (Figure 1b-d). However, on a local scale, high-resolution bathymetry details, especially the slope near the shelf break, played an important role in the generation of internal tides, which could be important in locations with large internal tide energy.

Globally there is a distinct signature of tidal variability, as can be seen from the kinetic energy of tidally forced HYCOM model simulations band-passed at semidiurnal (lunar) tidal frequencies (Figure 2a) and at higher frequencies, called supertidal frequencies (Figure 2b). The distribution of internal wave energy in the ocean is uneven, with extremes near generation sites such as coastlines and steep bathymetry, such as the Luzon Strait, (Figure 2d), a strait between Taiwan and Luzon, Philippines, a region of well-known for its strong internal tidal generation (e.g., Alford et al., 2015).

To assess how tidally forced models may differ acoustically from those without tides in locations such as these, we used a series of global HYCOM simulations: with or without tidal forcing and with or without data assimilation (DA). These experiments are summarized as tidal forcing and no DA (Exp. 19.0), no tidal forcing and no DA (Exp. 19.2), tidal forcing and DA (Exp. 21.6), no tidal forcing and no DA (Exp. 19.1), where the numbers correspond to saved experimental set-ups (e.g., https://hycom.org). Each was forced by wind and has a 1/25° (2-4 km) horizontal resolution and 41 layers. Hourly output was saved for each of these experiments for one month from May to June 2019. For each model iteration temperature and salinity were interpolated from the native grid to 101-depth layers and then used to compute sound-speed. Using a 5000 km transect across the Luzon Strait (Figure 2d) as an example, the depth of a single sound speed surface, 1510 m s^{-1}, is shown in Figure 2e. At the ridge, located at 1000 km along the transect, internal tides propagate in both directions, which can be seen in the depth change of this surface over time in the tidally-forced HYCOM simulation (Figure 2e). These are absent in the simulation without tides (Figure 2f). Steep topography in the North Pacific causes additional internal tide generation along this transect that is visible in the periodicity of the depth of the sound-speed surface at additional ridge locations (e.g., at 4800 km). Again, these undulations are absent in the simulation without tidal forcing.

Just as SSH spectral slope was compared to observations (i.e., Figure 1), it is also important to compare the sound speed in the simulations to observations, such as by examining sound speed variability at a single location. Here, the four simulations (with/without tides and with/without data assimilation) were compared to Spray glider observations in the California Current in the North Pacific (Figure 2c; Rudnick, 2016). The mean and standard deviation of the sound speed were computed from each simulation at 3-hourly intervals over the region that the glider was profiling. (The glider profiles from the surface to 500 m depth roughly every three hours.) Although this is not a region of large tidal energy, the tidal forcing still increased the sound speed variability. The simulation with both tidal forcing and data assimilation compared the closest to the observations. However, even without data assimilation, the HYCOM simulation with tidal inclusion lay closer to observations than the simulation without tidal forcing (Figure 2c).

Although the data-assimilative simulations of sound speed variability were closer to observations, implausible jumps can occur in the sound-speed structure during an assimilation window. Data-assimilation can abruptly alter the vertical temperature and salinity structure. It's unclear if the increase of sound speed variability in the data assimilative models was due to natural ocean variability or the assimilative 'shock' bringing the ocean closer to observations. These 'shocks' bring the ocean out of geostrophic balance (i.e., the balance between horizontal pressure gradients and rotation is disturbed). In the ensuing geostrophic adjustment process, in which the ocean tries to restore this balance, spurious low-mode internal waves are generated (Raja et al., 2024). These waves have frequencies that overlap with the tidal and inertial bands, complicating the analysis of naturally occurring tidal and near-inertial waves. For this reason, most of our HYCOM internal tide and IGW studies (e.g., Buijsman et al., 2020; Luecke et al., 2020; Raja et al., 2022; Arbic et al., 2022; Arbic 2022) have used HYCOM simulations without data assimilation. The interaction of these spurious IGWs with other internal waves or eddies and their eventual dissipation alters the ocean energetics. Hence, for much of the research during this project we used non-assimilative HYCOM simulations.

3. Amazon Region: A case study on IGW energy transfer and acoustic impacts

In the open ocean, low-mode internal tides (e.g., first baroclinic mode) may decay via wave-wave interactions that cascade energy to higher frequencies and wavenumbers (Lamb 2004; Eden et al., 2020). The energy at these primary frequencies, such as the diurnal and semidiurnal bands, dominate most of the internal tide spectrum, except along the path of large amplitude internal tides near the equator. Most of the research on IGW-IGW interactions in the open ocean has focused on subharmonic resonance, also called Parametric *Subharmonic* Instabilities, which transfer energy from tidal to *lower* 'subharmonic' frequencies (e.g., Ansong et al. 2018). In contrast, the decay of the low-mode internal tide due to *superharmonic* wave-wave interactions (interactions that transfer energy to higher than tidal frequencies), have not been thoroughly studied in global simulations. For this project, Solano et al. (2023) evaluated the energy transfers between tidal and supertidal frequencies and the interactions between low-mode waves in global HYCOM simulations.

Globally, higher-harmonic (supertidal) kinetic energy (KE) accounts for a significant portion of the total internal gravity wave energy, especially at low-latitudes. Band-pass filtering the HYCOM KE at supertidal frequencies (Figure 2b) shows that supertidal KE energy is higher at low-latitudes (<25°), propagating from 'hot spots' such as the Amazon Shelf. Supertidal energy accounts for about 5% of the total (tidal+supertidal) IGW energy, and internal tides transfer energy to higher harmonics at a rate of about 45 GW, compared to the 500 GW of energy available from barotropic tides (i.e., barotropic to baroclinic conversion). Locally, in regions such as the Bay of Bengal, the Amazon Shelf, and the Mascarene Ridge, 25-50% of the IGW KE is found at supertidal frequencies.

We focused on the two regions of high supertidal frequency: the Amazon Shelf and the Mascarene Ridge (Figure 3). The nonlinear IGW energy transfer from primary to supertidal frequencies revealed a banding pattern (Figure 3a-b) that agreed well with the horizontal divergence of the supertidal energy flux (Figure 3c-d). Where the supertidal energy was high, a regularly spaced banding pattern emerged where energy was transferred from primary to higher-harmonic frequencies at a rate of about 10-50 mW m^{-2} locally. The banding pattern in Figure 3 suggested a common mechanism for the nonlinear energy transfer between length scales. Decomposing the energy into separate modes (Figure 3e-f) shows that the banding pattern appeared when superimposing the lowest modes (1+2) but it was not present for individual modes. This suggests that these regions of enhanced energy transfer to higher-harmonics can be explained by the interactions between mode-1 and mode-2 internal tides, which interfere constructively at the locations of the patches (e.g., their velocities are in phase, increasing the tidal amplitude and steepening the internal tide). The location of these patches was modulated by the slowly varying subtidal current and the spring-neap cycle, with higher amplitude spring tides resulting in greater energy available to transfer to higher-harmonics.

The evidence of low to high mode IGW energy transfer make the Amazon basin and Mascarene Ridge interesting regions to examine the impact of tidal forcing on acoustic propagation. It was hypothesized that these active regions would strongly undulate the upper ocean, impacting both sound speed and its gradients. Along the Amazon shelf we examined the sound speed differences between tides and no-tides HYCOM simulations, and the impacts of tides on midfrequency acoustic propagation in and above the thermocline. In Section 4, the Mascarene Ridge is used to assess how model grid spacing and physics may cause differing acoustic variability.

In the Amazon region, semidiurnal internal tides propagate in a northeast direction away from the coast as be the regions of energy transfer in Figure 2. Sound speed, acoustic parameters and acoustic transmission loss were examined along this line, in a 60º radial along the direction of tidal propagation, as shown by a line in Figure 3a. First, we took the mean and standard deviation of sound speed in the upper ocean (Figure 3g, h) for both the tidal and non-tidally forced HYCOM simulations for one week, May 20-28. Although the mean sound speed was similar, there are notable differences in the thermocline (~150 m depth), where in the tidal case a similar “banding” of sound speed variability is observed to that of internal wave energy transfer (Figure 3a).

A virtual acoustic source was placed in the HYCOM simulations with and without tidal forcing at 4.1ºN and 44.8ºW and 20 m depth (Figure 3a; yellow star). For the acoustic model, we used a 1500 Hz source and a three-dimensional ray-tracing model, Bellhop 3D, available from the Ocean Acoustics Laboratory (Porter, 2011). Running an acoustic propagation model provides direct information of how sound at a given frequency and depth may propagate. We used acoustic transmission loss (TL) to provide a relative estimate of acoustic pressure, a proxy of how detectable a source may be at a certain range. A snapshot of the sound speed structure along this 60º radial line shows undulations in the tidal case that were absent in the nontidal case (Figure 4a, top panels). The internal tides oscillate the pycnocline thus changing both the vertical and horizontal sound speed gradients (Figure 4a(i, ii)). At this time step, the tidal case showed greater transmission loss in the surface layer, whereas strong transmission occurred in the nontidal case (Figure 4a, bottom panels).

Acoustic parameters can be used to quantify the differences between the tidal and non-tidal ocean simulations. When examining the properties of potential surface duct propagation in the upper ocean, as we are here, two acoustic parameters of interest are the sonic layer depth (SLD) and below-layer gradient (BLG). The SLD is defined as the depth of the subsurface sound-speed maximum (e.g., Helber et al., 2008). If the acoustic source is within the layer and the frequency is supported by the layer, sound can potentially be trapped between the surface and the SLD. The BLG, defined as the gradient in sound speed below the SLD, can influence the potential of the layer to retain trapped energy. Comparing the tidal and nontidal snapshots, the SLD was shallower and the BLG more variable in the HYCOM simulation forced with tides than that without tidal forcing. The structure of the sound speed profiles (horizontally and vertically) also guide the paths of the sound. A smooth profile will result in a greater concentration of energy (less loss) and a profile with many small gradient variations will result in more refracted energy (more loss) throughout the entirety of the waveguide.

A timeseries of TL, SLD and BLG showed the persistent differences between the HYCOM simulations with and without tidal forcing. In the tidal case TL was greater, likely because of a shallower SLD, particularly from 20 to 23 May. The transmission was sensitive to this depth, with transmission occurring on a semidiurnal timescale (e.g., every 12 hours) with the upper ocean undulation. In the nontidal case, there were no periodic fluctuations of TL, only irregular fluctuations associated with submesoscale to mesoscale variability. The relationship between SLD and TL thus appeared relatively straight forward, with poor transmission if the source is positioned below the SLD. Less clear was the relationship of TL to BLG, which was more variable in the tidal case (Figure 4b), or the relationship of TL to the horizontal sound speed gradients introduced by tidal forcing.

The mesoscale differences between the tidal and non-tidal HYCOM simulations made a direct comparison between them problematic, and later impacted how DL parameterizations were made (Section 5). Some of this variability was owing to how the tides interact with the mesoscale field and atmospheric forcing. Correlation coefficients between wind and mixed layer depths in the Amazon region were similar between the tides and no-tides simulations, but with differences near the coast where currents and tidal variability were strong. This will be an avenue of future research, but it made linking the relative amplitude of the tidal energy to acoustic impacts difficult.

4. Horizontal and vertical grid spacing

Horizontal and vertical grid spacing, as well as the parameterizations commonly used to represent unresolved processes in ocean models, significantly impact the ability of models to represent internal tides and IGW processes (Nelson et al., 2020; Buijsman et al., 2020; Kelly et al., 2021; Thakur et al., 2022). The grid spacing also affects temperature and salinity distributions and thus acoustic propagation. During this project, horizontal grid spacings of 2-4 km were used for HYCOM (as seen in the previous section), which is a finer grid spacing than 1/12º grid spacing available in many global ocean models. There is a clear link between the HYCOM grid spacing and the magnitude of the semidiurnal internal wave energy (Buijsman et al., 2020). For example, decreasing the horizontal grid size from 8 to 4 km increases the internal wave generation and energy density by about 50%. This is largely because of the number of internal wave modes resolved, increasing from the first two modes in the 8-km simulation to the first 4 modes in the 4-km simulation.

The horizontal and vertical grid spacings determine how well vertical features of bathymetry and, respectively, horizontal and vertical wavelengths of the modes are resolved. Both the modal wavelengths and grid spacings are spatially variable in global ocean models. For example, the horizontal grid spacing generally decreases poleward due to the sphericity of the earth, while the wavelengths of tidally generated internal waves increase poleward due to the increase of the Coriolis frequency. We applied existing and newly developed criteria to determine what diurnal, semidiurnal, and supertidal vertical wave modes could be resolved depending on both the horizontal and vertical resolution of the 4-km global HYCOM simulation with 41 layers (Figure 5; Exp. 19.0). For the horizontal resolution we used the criterion that a vertical mode is resolved if there were at least 6-8 horizontal grid spacings per wavelength (Steward et al., 2017). A similar criterion was applied for the vertical resolution (vertical criterion CZA). However, this criterion is designed for *z*-coordinate models, whereas HYCOM is an isopycnal model below the mixed layer. Therefore, we applied an additional criterion called CZB, which accounted for both the vertical and horizontal velocity structure. The goal was to see how modes could be resolved globally using these criteria.

The zonal mean of the number of the resolved modes for seafloor depths >2000 m and averaged over 10° latitude bins is presented in Figure 5a. Internal wave modes with lower frequencies have longer wavelengths, and hence, they are better resolved by the horizontal resolution. For example, for the lunisolar diurnal internal tide, K_1, around eight modes are resolved at the equator and the number increases towards 20 modes near the K_1 turning latitude of about 30º due to the increase in wavelength. Poleward of this latitude, the tidal frequency is smaller than the Coriolis frequency, and diurnal internal waves cannot exist. The shorter wavelength principal lunar semidiurnal internal tide, M_2, had fewer modes resolved, with a minimum number of about four modes resolved at the equator. Supertidal internal tidal waves occur at higher harmonics of the primary tidal frequencies, as discussed in the previous section. Globally, the supertidal waves with the quarter diurnal M_4 frequency have the most energy (see Figure 1 of Solano et al., 2023). On average, only up to two M_4 modes were resolved. The number of resolved modes was more sensitive to the vertical resolution criteria than to the horizontal resolution. If CZA was applied to the hybrid vertical coordinates, mode-1 is barely resolved at the low latitudes and not at all at higher latitudes (Figure 5a). In contrast, CZB appeared to be a more appropriate criteria, and allowed for the resolution of more modes with a maximum of 12 diurnal modes resolved at the equator. Having criteria for how many modes may be resolved in a global model with a certain discretization will help interpret the meaning both of internal tidal energy transfer and the sound speed variability.

Grid spacing does have a direct impact on sound speed variability, as smaller grid spacing may resolve more processes and stronger temperature and salinity gradients. As an example, we compared SLD and BLG at the Mascarene Ridge between a two-dimensional nonhydrostatic simulation of the MITgcm, with a horizontal grid spacing of 100 m, to the simulations of the tidally forced global HYCOM model (Exp. 19.0), which is hydrostatic and has a horizontal grid spacing forty-times greater than that of the MITgcm simulation (Figure 5b, c). The Mascarene Ridge is a location of nonlinear wave interactions, where solitons are generated and propagate away from the Ridge (Figure 3b, d, f). Although a direct comparison of the sound-speed structure was not possible, as the HYCOM simulations were initialized with an offset in temperature, a relative comparison of these acoustic parameters was insightful (Figure 5b, c). The HYCOM simulation had semidiurnal fluctuations of the SLD and BLG, with each oscillating twice a day (Figure 5b). The MITgcm simulation had a periodic signal as well, but it was disorganized, with propagation pathways appearing to overlap (Figure 5c). The closer grid spacing of the MITgcm simulation likely allowed for nonlinear interactions to occur between different internal waves which in turn impacted the sound speed structure. This structure is likely more realistic when compared to observed ocean variability, but it would also make the sound speed less predictable.

With the increase in computational power, more submesoscale-resolving regional and basin-scale models have been developed in the past years, such as the 1-km grid-spacing HYCOM simulation for the Gulf of Mexico (Chassignet and Xu, 2017; Hiron et al., 2021, 2022; Chassignet et al., 2023). Ongoing discussions within the oceanography community resolve around performing global HYCOM simulations with tides with a finer grid-spacing on the order of 1/50º (the most up-to-date global HYCOM has 1/25º grid-spacing). However, the optimal number of vertical layers needed in submesoscale resolving models to resolve internal tides and tidal energetics, and the consequent effect on acoustic propagation is still an open question. To explore this question, we used an idealized HYCOM configuration with 1/100º horizontal grid-spacing (1 km), forced only by the semidiurnal (M_2) tides over a centrally spaced ridge, and varied the number of layers between the simulations from 8- to 128- layers (Figure 6). The idealized configuration allowed the problem to be isolated from contamination by ocean eddies and currents while resolving all the physics allowed in HYCOM.

Each simulation was initialized with a climatological temperature profile averaged over the Cape Verde area and a constant salinity structure. The domain size, approximately 8000 km in the zonal direction, was large enough to prevent the reflection of internal tides at the boundaries. The vertical grid-discretization of these layers was chosen based on characteristic wavelengths of different IGW modes. To generate internal tides, a steep ridge with a Gaussian shape was added in the center of the domain. The criticality of the slope, which is a measure of the ridge steepness normalized by the ray slope of the internal waves, was larger than one, allowing for the generation of nonlinear waves and wave beams (Garrett and Kunze, 2007; Buijsman et al., 2010). Figure 6a is a snapshot of the vertical velocity for the 128-layer simulation, highlighting the region near the ridge where the wave beams were the strongest. Figure 6b shows the depth-integrated, vertical KE ($\frac{1}{2} \int w^2 dz$), where w is the vertical velocity, for different vertical discretizations (8-, 16-, 32-, 48-, 64-, 96-, and 128-layer) and averaged over one week. The vertical KE of the 8- and 16-layer simulations differed from the others in amplitude and phase. As the number of layers increased, the simulations became more similar, both in amplitude and phase. From the 48- to the 128-layer simulations, magnitude and phase are similar across simulations. Strong vertical velocities led to greater vertical displacement of the isopycnals which can then affect sound speed and, potentially, acoustic propagation. When integrated over the whole domain (0 to 2000 km from the ridge), the tidal barotropic-to-baroclinic energy conversion, the vertical kinetic energy, and the turbulent dissipation were greatest in the 128-layer simulation and decreased with coarser vertical grid spacing. The results started to converge for the simulations with more than 48 layers, however, these results may differ with a change in horizontal grid spacing.

The idealized model can be used to isolate the possible impact of vertical grid spacing on sound speed, without the confounding challenges of differences in mesoscale eddy fields or initialization states such as in the examples of the Amazon basin and Mascarene ridge. We interpolated the 8-, 16-, 32-, 48-, and 96-isopycnal layer simulations each to constant-depth coordinates, then took the mean and standard deviation of sound speed over 72-hourly timestep (Figure 6c, d). The lower vertical grid simulations (less than 32-layers) had greater mean sound speeds and deeper SLDs (Figure 6c). These lower-layer simulations had some difficulty resolving the locations of large sound speed variability (Figure 6d), which would likely impact acoustic propagation. As the number of layers increased, the sound-speed profiles and their variability converged with very little difference between the 48- and 96-layer simulations. Hence, the number of layers affected the simulation of internal tides, with a minimum of 48 isopycnal layers (for a 1 km horizontal grid-spacing) necessary to ensure an accurate representation of internal tide-induced isopycnal displacement. A similar impact was observed for the mean sound speed and its variability, with 48-layers or greater needed to converge on similar results.

5. A final word on energetics

The IGW spectrum covers both the transfer of energy between internal wave modes and the transfer of oceanic kinetic energy from its injection at large scales in eddies, near-inertial-waves, and tides to the smallest scales. As such, properties of the IGW spectrum depend on the ocean state, including the slowly varying background circulation and surface forcing that may affect vertical stratification. An empirically determined form of the IGW spectrum, determined by Garrett and Munk (1979), is applicable globally but uses free parameters to account for regional and seasonal variations. Ongoing research focuses on what determines these parameters and any deviation from this spectral form; nonlinear interactions involving IGWs, such as those on display in the Amazon basin and near Mascarene Ridge, are thought to be of particular importance.

Previous theoretical and idealized work on IGW-IGW interactions has identified some important processes that move energy to smaller scales (McComas and Bretherton, 1977; Dematteis et al., 2022). These studies did not analyze eddy-IGW interactions in the same manner as IGW-IGW interactions and considered the latter to be the dominant processes. One IGW-IGW mechanism involving the interaction of near inertial and tidal IGWs, called “induced diffusion”, is thought to be very important in transferring KE across length scales. Skitka et al. (2024) used a unique framework to diagnose these IGW-IGW interactions along with analogous eddy-IGW interactions from a regional MITgcm ocean simulation in the North Pacific (Nelson et al., 2020;

Pan et al., 2020, Thakur et al., 2022). They found that IGW-eddy interactions induce a downscale KE flux in a manner analogous to IGW-IGW interactions. This "eddy-induced diffusion" is the dominant mechanism of energy exchange within the IGW supertidal continuum at 2-km horizontal grid spacing, which is typical grid spacing for the highest-resolution global models that can presently be run, and is achievable in the HYCOM simulations used here. This "eddy-induced diffusion" is comparable to the wave-induced diffusion at the higher 250-m horizontal grid spacing that is achievable by regional models. Thus, the finer grid spacing in the vertical and horizontal directions will make a large difference in the details of the IGW cascade, including the rate of energy transfer, the dominant mechanisms that contribute to it, and the mechanisms and patterns of dissipation. All of these have implications for the ability of global models to resolve oceanic processes and thus sound speed and its variability.

6. Developing awareness and creating solutions using Deep Learning (DL)

It is clear from the work thus far that the inclusion of tidal forcing in ocean simulations increases the realism of the ocean state, as do finer grid spacing in both the vertical and horizontal. However, tidally forced, global ocean models are computationally expensive, especially those with fine grid spacing. DL was used to investigate the statistical differences between HYCOM simulations with and without tidal forcing. The goal was to generate a tidally forced ocean state from a non-tidally forced HYCOM simulation without numerically solving the physical forcing equations, both to reduce the computational cost and to more rapidly predict acoustic impacts.

A Generative Adversarial Network (GAN; Goodfellow et al., 2014; Creswell et al., 2018) was proposed as a potential solution, using the simulations of global HYCOM with and without tides (Exp. 19.0) as initialization states. General Adversarial Networks (GANs) are a DL technique that tries to learn a transformation from one statistical distribution to another, instead of trying to directly learn a specific distribution. The DL model is trained alongside an adversarial discriminator, which is a classifier used to differentiate between actual data and generated data (Goodfellow et al. 2014, Goodfellow et al. 2016). Given this formulation, GANs are well suited to translate nontidal results to tidal results for vice versa.

To address this issue of the chaotic, turbulent nature of the ocean we considered the HYCOM simulations with and without tidal forcing to be unpaired. This meant that we did not compare a specific point in space and time between the two simulations. As we considered this data unpaired, we trained the networks in a way that compares the simulations using cycle-consistency loss. For this method, we trained two separate generators and discriminators. One generator, $G_{NT \to T}(\cdot)$, translates from the non-tidal to the tidal domain, and the other generator, $G_{T \to NT}(\cdot)$, translates from the tidal to non-tidal domain. For training, data was translated to the opposite domain, and then translated back to the original domain. The cycle-consistency loss is defined as the mean-squared difference between the original data sample and the doubly translated data (Zhu et al., 2017). The cycle-consistency loss was then used in combination with the traditional GAN losses to train the networks.

The Atlantic Ocean was used as a test-case region and split into 90% training data and 10% validation data. Figure 7 shows some examples of the results, with the original HYCOM model simulations with tides (Exp 19.0) and without tides (Exp. 19.2) and GAN outputs for selected samples in the validation set. The example subfigures are time series at each given location (Figure 7a), representing samples of how the GAN network performs in different oceanographic conditions.

The general structure of the temperature and salinity profiles was retained in the GAN translation. For example, south of New England in the Gulf Stream (Figure 7b), the tidally forced observations had a fresher, cooler region extending to 150 m depth that dissipated after approximately 90 hours. This was likely a mesoscale intrusion and was absent in the nontidal results. Thus, it was poorly represented when comparing the original tidally forced HYCOM to the GAN generated tidal fields. The GAN model captured the periodic structure consistent with tidally forced simulations which varied depending on the sample location. The DL model handled these differences consistently. For instance, in the mid-Atlantic (Figure 7c), there were periodic signatures in temperature, salinity and velocity. Here, the periodicity of the outputs of $G_{NT \to T}(\cdot)$ matched nicely with those from HYCOM with tides. It was more difficult to separate the mesoscale variability from the tidal structure in the Gulf Stream (Figure 7d). The DL model artificially increased the periodic structure (most visible in water velocity). This location, further from the shore than that of 7b, likely was dominated by a strong mesoscale eddy field. This was an instance where the DL model imposed a periodicity to make the sample like other tidally forced results, even though the actual HYCOM sample did not contain this structure.

As the data we utilized was unpaired, it is difficult to evaluate the performance of the model without visually inspecting the outputs. In future work, a discriminator could be trained to differentiate between these results. Because the model output used to train the DL models were sampled from a region of the globe during the same time of year, no two samples were completely independent. This introduces the risk of overfitting. Using unpaired data made the model more robust to overfitting but did not remove the risk entirely. Additionally, the sound speed structure had a persistent offset of about 5 m/s greater in the GAN generated results than the original HYCOM simulations (not shown). Thus, although this work provides a good starting point, further work is necessary to improve the DL approach.

7. Conclusions

The TFO-HYCOM project was a cross-disciplinary investigation into the modeling of internal tides and high-frequency IGWs, their sensitivity to model horizontal and vertical grid spacing, the energy transfer and dissipation of IGWs, the impacts on sound speed structure and acoustic propagation, and the ability to replicate tidal simulations using DL techniques. During this project we examined the sensitivity of modeled IGWs to bathymetry and damping schemes and compared them to observations.

The inclusion of tidal forcing in ocean models improves the representation of the ocean state. Tidal forcing has a direct impact on acoustic propagation via changes that it induces to the sound speed at scales from kilometers to hundreds of kilometers, and time scales on the order of a few to several hours. HYCOM simulations run with and without tides showed clear differences in mean sound-speed structure and sound-speed variance, that was evident both in mesoscale features and at tidal frequencies. Simulations that included tidal forcing tended to have greater sound-speed variance and were more consistent with observations. These impacts were sensitive to vertical and horizontal discretization, as were the ability of the simulations to resolve IGW interactions and energy transfer. In addition to the tilt of density surfaces caused by internal waves, spice, temperature and salinity fluctuations along a constant density surface, can have a similarly large impact on sound speed and its gradients (Dzieciuch et al., 2004; Colosi et al., 2012). Spiciness, is caused by ocean stirring by mesoscale eddies. Although we do not separate out the effects of spice from isopycnal tilt here, it's likely spice would also differ between the models as IGWs interact with the mesoscale field. Further investigations into acoustic impacts could also be made by looking at different frequency ranges or acoustic arrival times, for example performing long-range, low-frequency acoustic propagation and comparing model results with observational studies (e.g., Dushaw et al. 2011).

As global operational models begin to include tidal forcing, along with a decrease in grid spacing, it is important to understand how well they represent physical processes and how energy cascades through the internal wave spectrum. As running these models at high resolution is computationally expensive, machine learning techniques may facilitate predictions of IGW impacts on ocean state using a model with coarser grid spacing or simulations without tidal forcing.

Acknowledgements:

This TFO-HYCOM project was funded by related Office of Naval Research (ONR) grants sent to the different institutions involved – N00014-19-1-2712 to University of Michigan, N00014-19-1-2717 to Florida State University, N00014-19-1-2704 to University of Southern Mississippi, N00014-20-C-2018 to ARiA and Applied Ocean Sciences, LLC, and contract number N00014-22WX00941 to the Naval Research Laboratory. We gratefully acknowledge ONR for their support of our research and thank the reviewers of this article for their helpful suggestions and insights.

Author information:

Martha C. Schönau was a Senior Scientist at Applied Ocean Sciences, LLC, and is now an Assistant Project Scientist at the Scripps Institution of Oceanography at the University of California San Diego.

Luna Hiron is a Postdoc at the Center for Ocean-Atmospheric Prediction Studies at Florida State University.

John Ragland was a summer intern at Applied Research in Acoustics, LLC (ARiA), and is a PhD student in the Department of Electrical and Computer Engineering at the University of Washington.

Keshav J. Raja is an Assistant Research Scientist at the Center for Ocean-Atmospheric Prediction Studies at Florida State University.

Joseph Skitka was a Postdoc at the Department of Earth and Environmental Sciences at the University of Michigan and is now a Postdoc in the Physical Oceanography department at Woods Hole Oceanographic Institution.

Miguel S. Solano was a Postdoc at the School of Ocean Science and Engineering at the University of Southern Mississippi and is now a Research Scientist at SOFAR Ocean Technologies.

Xiaobiao Xu is a Senior Research Scientist at the Center for Ocean-Atmospheric Prediction Studies at Florida State University.

Brian K. Arbic is a Professor in the Department of Earth and Environmental Sciences at the University of Michigan.

Maarten C. Buijsman is an Associate Professor at the School of Ocean Science and Engineering at the University of Southern Mississippi.

Eric P. Chassignet is a Professor and Director of the Center for Ocean-Atmospheric Prediction Studies at Florida State University

Emanuel Coelho is Chief Scientist at Applied Ocean Sciences, LLC.

Robert W. Helber is an Oceanographer for the Naval Research Laboratory at the Stennis Space Center in Mississippi.

William Peria is a Senior Research and Development Scientist at Applied Research in Acoustics, LLC (ARiA).

Jay F. Shriver is an Oceanographer for the Naval Research Laboratory at the Stennis Space Center in Mississippi.

Jason Summers is the Chief Scientist at Applied Research in Acoustics, LLC (ARiA).

Kathryn L. Verlinden is a Senior Scientist at Applied Ocean Sciences, LLC (AOS).

Alan J. Wallcraft is a Research Scientist at the Center for Ocean-Atmospheric Prediction Studies at Florida State University.

Author Contributions

This manuscript highlights the research efforts by postdocs and early career researchers on the TFO-HYCOM project. The TFO-HYCOM team that focused on improving IGW modeling was composed of researchers from the Naval Research Laboratory (NRL), Florida State University (FSU), The University of Southern Mississippi (USM), and University of Michigan (U-M), each with a complementary research focus for the project. The NRL team provided global HYCOM simulations at 1/25º horizontal grid spacing. FSU researchers performed higher horizontal grid spacing (1/50º) North Atlantic basin simulations and idealized simulations with finer horizontal and vertical grid spacing (1 km and up to 128 vertical layers) to study the impact of vertical, horizontal, and bathymetry grid spacing, tidal forcing, and data assimilation on IGWs in HYCOM. USM researchers examined kinetic energy content and transfer between different IGW modes and provided MITgcm simulations along the Mascarene Ridge, while U-M researchers further examined the theory of IGW nonlinear energy transfer and dissipation in very-high-resolution regional simulations of the MITgcm. Researchers from NRL and Applied Ocean Sciences (AOS) used the global HYCOM model simulations with and without tidal forcing to assess the impact of tidal forcing on acoustic prediction parameters and acoustic transmission loss. AOS also looked at acoustic propagation in the idealized models and the MITgcm. Finally, researchers from Applied Research in Acoustics (ARiA) used deep learning (DL) algorithms to derive a tidal ocean state from HYCOM model results without tidal forcing to reduce computational costs.

Martha C. Schönau was the lead writer of this manuscript, project lead at her institution, and performed the research contributing to Figures 3g,h, 4, 5b,c, and 7a. Figures and research were also contributed by Maarten Buijsman (Figure 5a), Luna Hiron (Figure 6), John Ragland and William Peria (Figure 7b-d), Keshav J. Raja (part of Section 2), Joseph Skitka (Section 5), Miguel S. Solano (Figures 2a, b and 3), Xiaobiao Xu (Figure 1), and Jay F. Shriver and Robert

W. Helber (Figure 2c-f). Brian K. Arbic, Maarten C. Buijsman, Eric P. Chassignet, Emanuel Coelho, Robert W. Helber, Jay F. Shriver, and Jason E. Summers served as co-PIs of this TFO-HYCOM project at their respective institutions and oversaw the research efforts. Arbic conceived the idea of a project on internal wave impacts on acoustics, co-led the proposal writing, and organized regular online group meetings. Summers co-led the proposal writing for the project and served as lead principal investigator. Kathryn L. Verlinden provided ocean-atmospheric analysis in the Amazon region. Alan J. Wallcraft helped guide and run the Florida State University basin-wide Atlantic HYCOM simulations.

Figures:

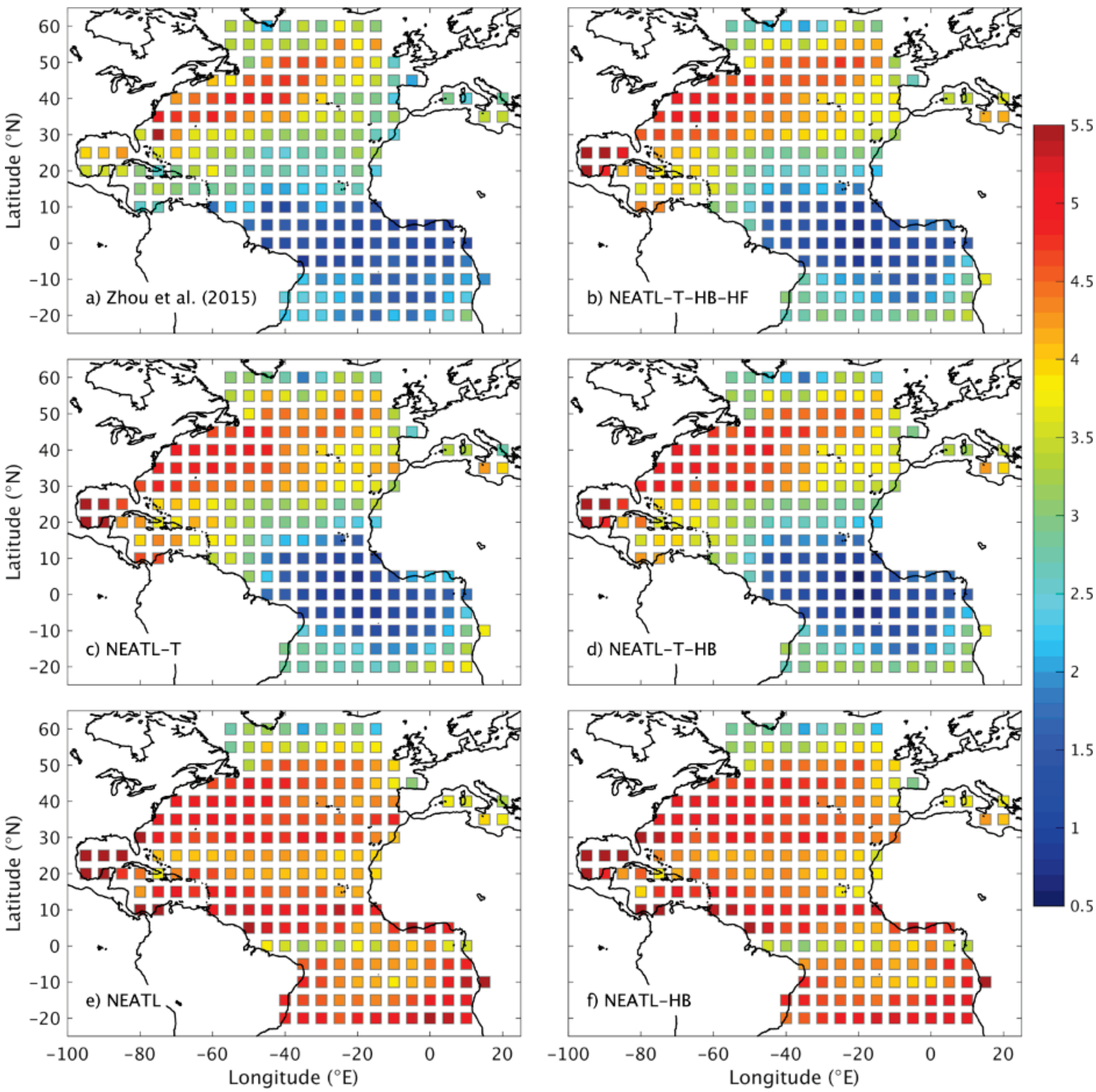

Figure 1. Mesoscale sea surface height (SSH) wavenumber spectral slope in the Atlantic Ocean based on (a) satellite observations and (b-f) a series of 1/50° numerical simulations (see Xu et al., 2022 for more detail). NEATL-T-HB-HF (with tides, high-resolution bathymetry, and high-frequency atmospheric forcing); NEATL-T (with tides); NEATL-T-HB (with tides, high-resolution bathymetry); NEATL (no tides); NEATL-HB (no tides, with high-resolution bathymetry). The result highlights that the large-scale spatial variability of the spectral slope is

primarily due to the internal tides, whereas the impact of high-resolution bathymetry (difference between c and d) and high-frequency atmospheric forcing (difference between b and d) is relatively small. Taken from Xu et al. 2022, Figure 7. **Printed with permission.**

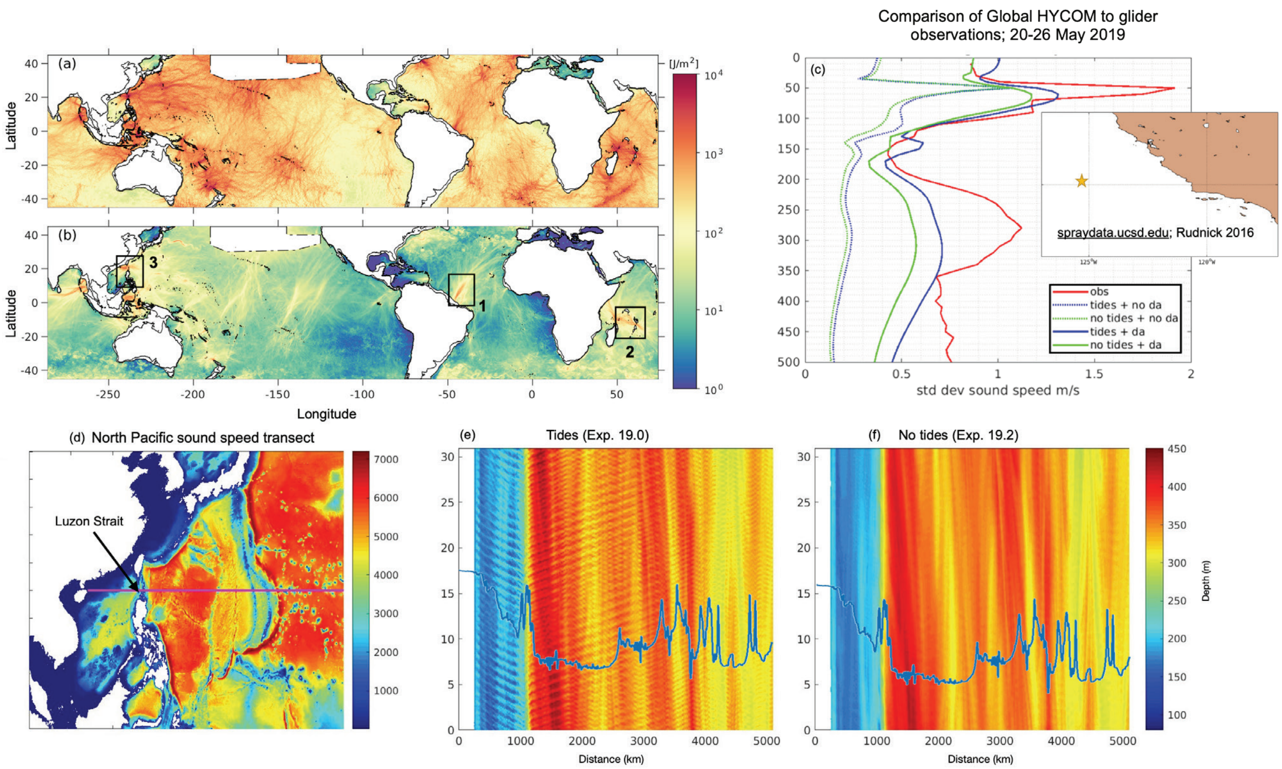

Figure 2: Time-mean and depth-integrated internal wave kinetic energy (J m^{-2}) band-passed at (a) semidiurnal and (b) supertidal frequency bands. Regions with relatively high supertidal energy used as examples are indicated by the black rectangles: (1) the Amazon Shelf, (2) the Mascarene Ridge and (3) the Luzon Strait. (c) Standard deviation of sound speed for 20-26 May 2019 from Global HYCOM simulations with and without tides and with and without data assimilation at location indicated on map of the coast of California. Simulations are compared to standard deviation computed from glider observations over the same week and location. (d) Map of transect (magenta line) from the South China sea to the North Pacific, bisecting the Luzon Strait. The depth of the 1510 m s^{-1} sound speed surface is shown along the transect shown in (d) for the HYCOM simulations (e) with tidal forcing (Exp. 19.0) and (f) without tidal forcing (Exp.

19.0). Bathymetry is overlaid on each (e) and (f), with the Luzon Strait is located at 1000 km distance.

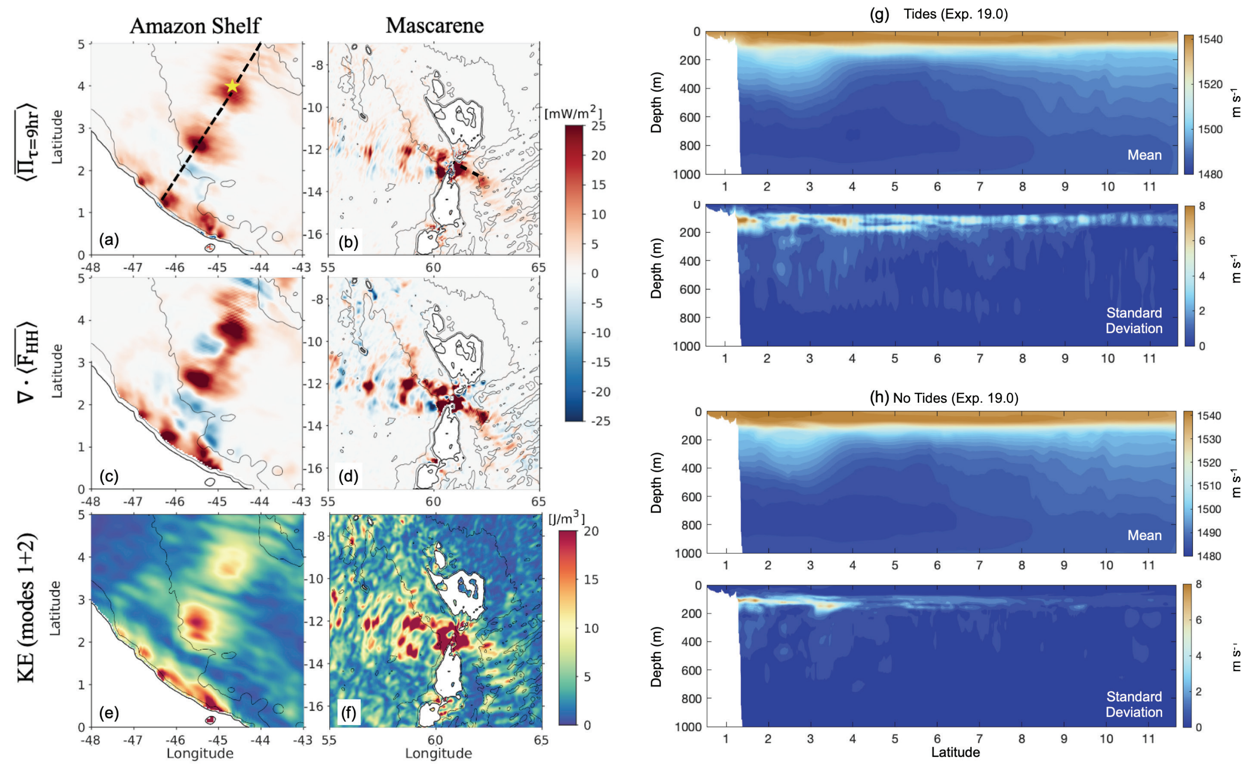

Figure 3. Time-mean and depth-integrated coarse-grained kinetic energy transfer ($\langle\Pi_{(\tau=9hr)}\rangle$) at the (a) Amazon Shelf and (b) Mascarene Ridge. Time-mean, depth-integrated divergence of supertidal energy flux ($\nabla\cdot\langle F_{HH}\rangle$) at the (c) Amazon Shelf and (d) Mascarene Ridge. Time-mean surface kinetic energy for the superposition of modes 1+2 at the surface at the (e) Amazon Shelf and (f) Mascarene Ridge. Panels (a)-(f) are modified from Solano et al. (2023). Sound speed mean and standard deviation for each the (g) tidal and (h) non-tidally forced HYCOM simulations from May 20-29, 2019, in the Amazon region, plotted by latitude along the dotted line shown in (a). In (a), the location of the acoustic source (star) and radial (dashed black line) used in Figure 4 are also noted. In (b), a short, dashed line indicates the transect used in Figures 5b and 5c.

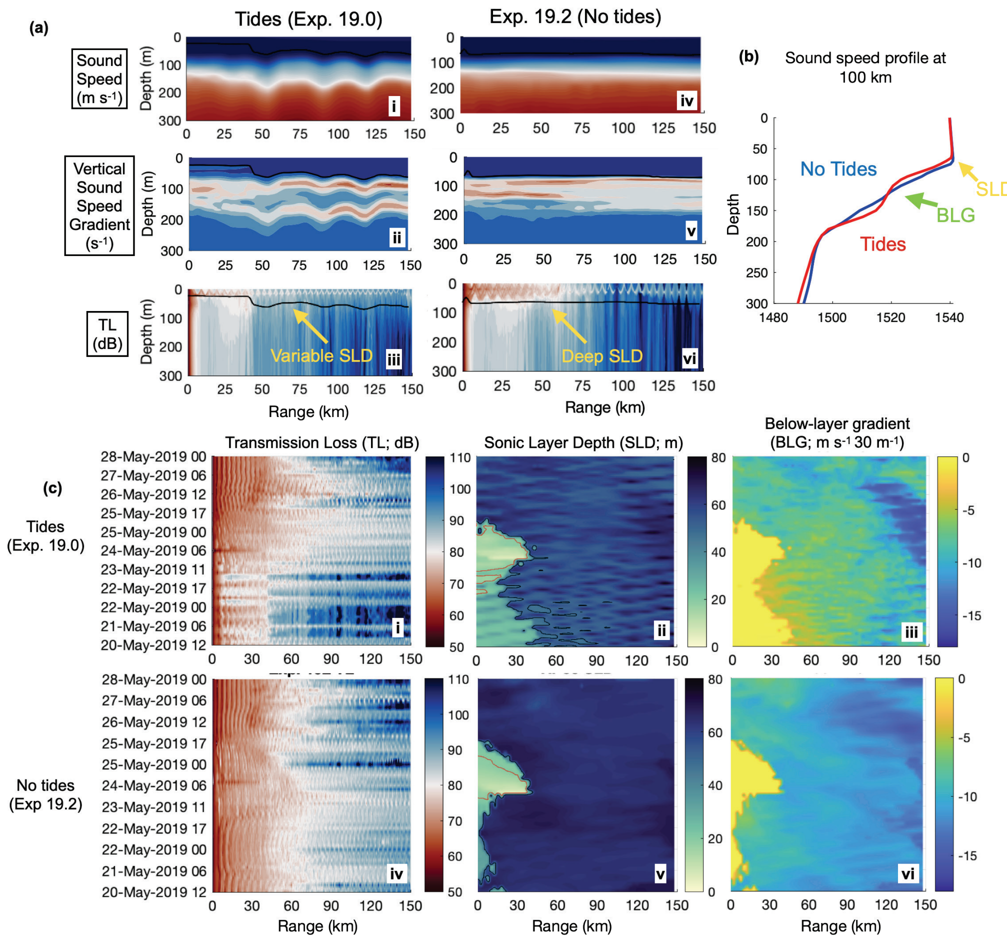

Figure 4: Comparison of acoustic propagation and properties between non-assimilative global HYCOM simulations with tidal forcing (Exp.19.0) and without tidal forcing (Exp.19.2). The location of the source and radial are indicated in Figure 2a, with acoustic propagation shown at 60º counterclockwise from east. (a) A snapshot from 20 May 2019 18:00:00 of (i, iv) sound speed (m s^{-1}) (ii, v) vertical gradient of sound speed (s^{-1}) and (iii,vi) TL (dB) for (i-iii) tidally forced and (iv-vi) non-tidally forced simulations. (b) Comparison of a single velocity profile at 100 km distance from the source along the 60º radial. (c) Acoustic transmission loss (TL) at 20 m depth, sonic layer depth (SLD) and below-layer gradient (BLG) along a radial 60º counterclockwise from east for a 1500 Hz source at 20 m depth located in at 4.1ºN and 44.8ºW for each (i-iii) a tidally (Exp. 19.0) and (iv-vi) a non-tidally (Exp. 19.2) forced HYCOM simulation.

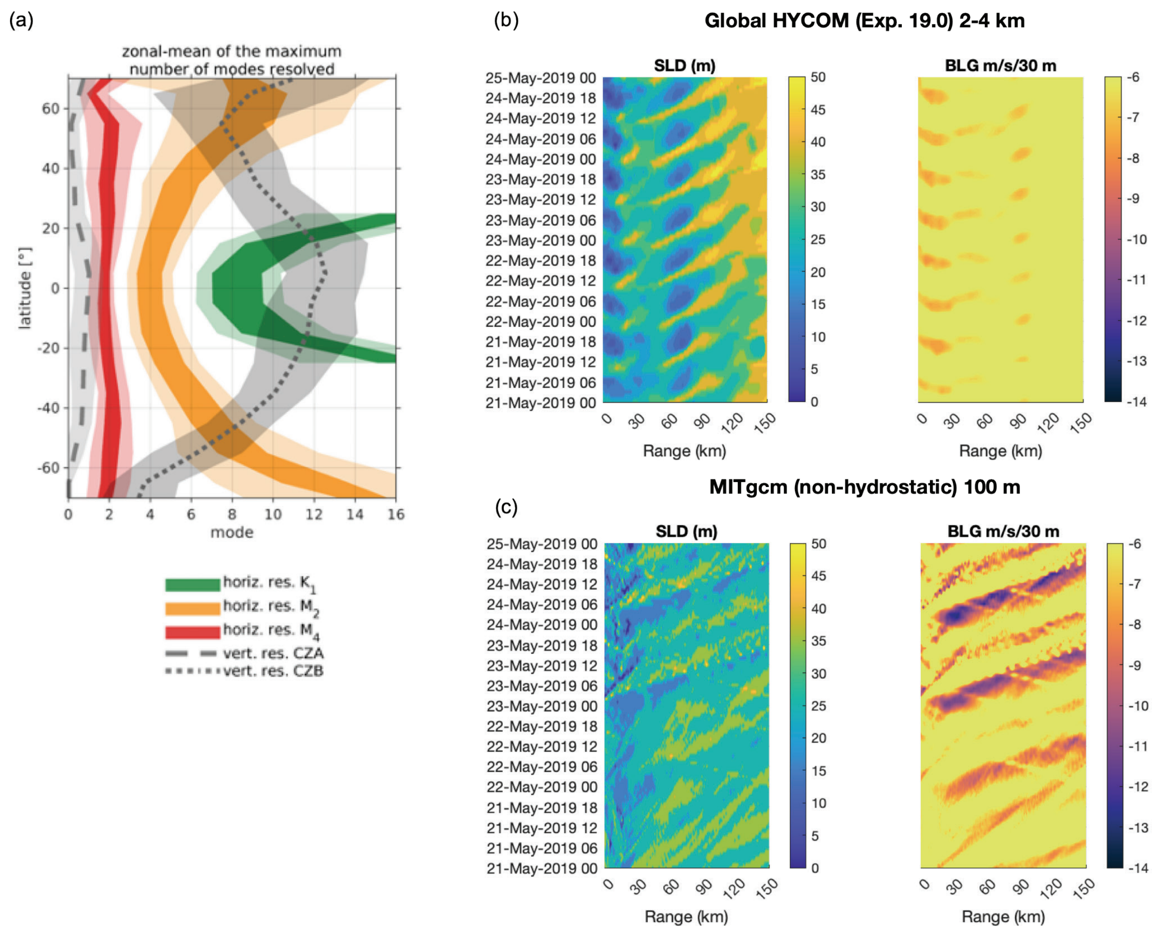

Figure 5. (a) The predicted number of modes resolved for the horizontal resolution for various internal tide frequencies (colored polygons) and the vertical resolution (gray shaded polygons) area-averaged over longitude and 10° latitude bins. K_1, M_2, M_4 represent the dominant diurnal, semidiurnal, and supertidal constituents of internal tides with decreasing wavelengths, respectively. For the horizontal resolution, the dark-colored polygons mark the range of the number of resolved modes bounded by 6 and 8 cells/wavelength and the light-colored polygons mark the extent of the zonal-mean ± 1 standard deviation. For the vertical resolution, the dashed lines mark the zonal-means and the gray-shaded polygons mark the extent of the zonal-mean ± 1 standard deviation. (b) SLD and BLG for global HYCOM simulation with tides (Exp 19.0) and (c) SLD and BLG for a nonhydrostatic regional MITgcm simulation near the Mascarene Ridge (see Figure 3b).

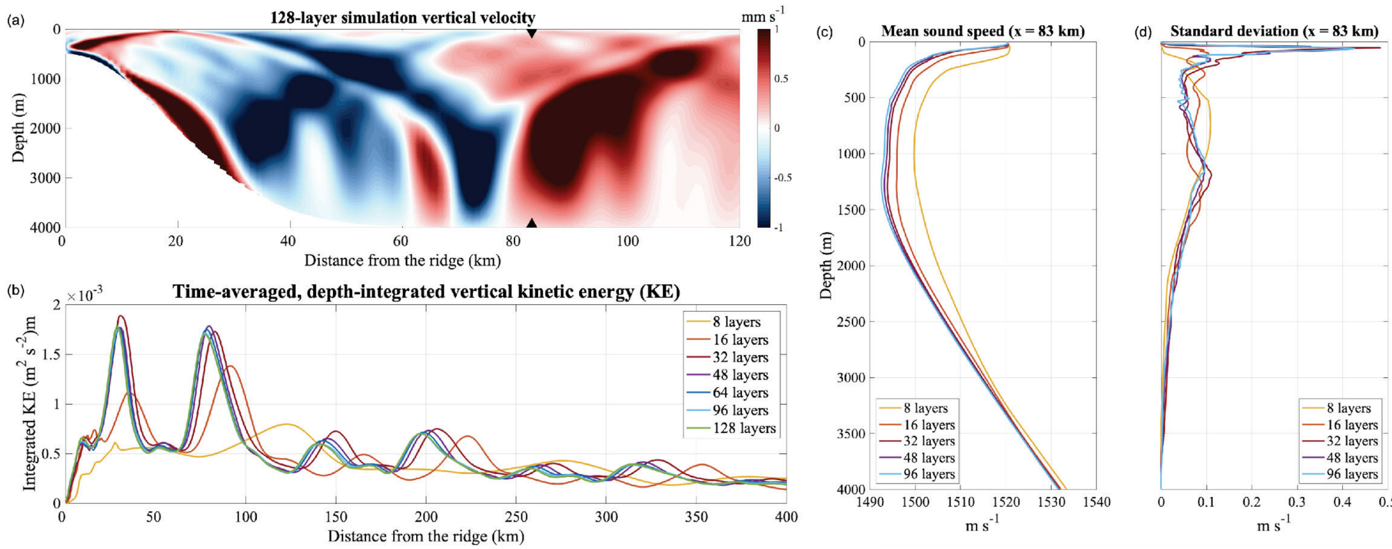

Figure 6. (a) Snapshot of the vertical velocity for the 128-layer simulation, zooming in closer to the ridge centered at 40ºW (the domain extended from 60ºW to 20ºW). The black triangles indicate the location where the sound speed profiles, shown in (c). (b) Time-averaged, depth-integrated vertical kinetic energy (½ $\int w^2 dz$), where w is the vertical velocity, for different vertical discretizations: 8-, 16-, 32-, 48-, 64-, 96-, and 128-layers. (c) Mean and standard deviation of sound speed 83 km from the ridge for 8-, 16-, 32-, 48-, and 96-layers.

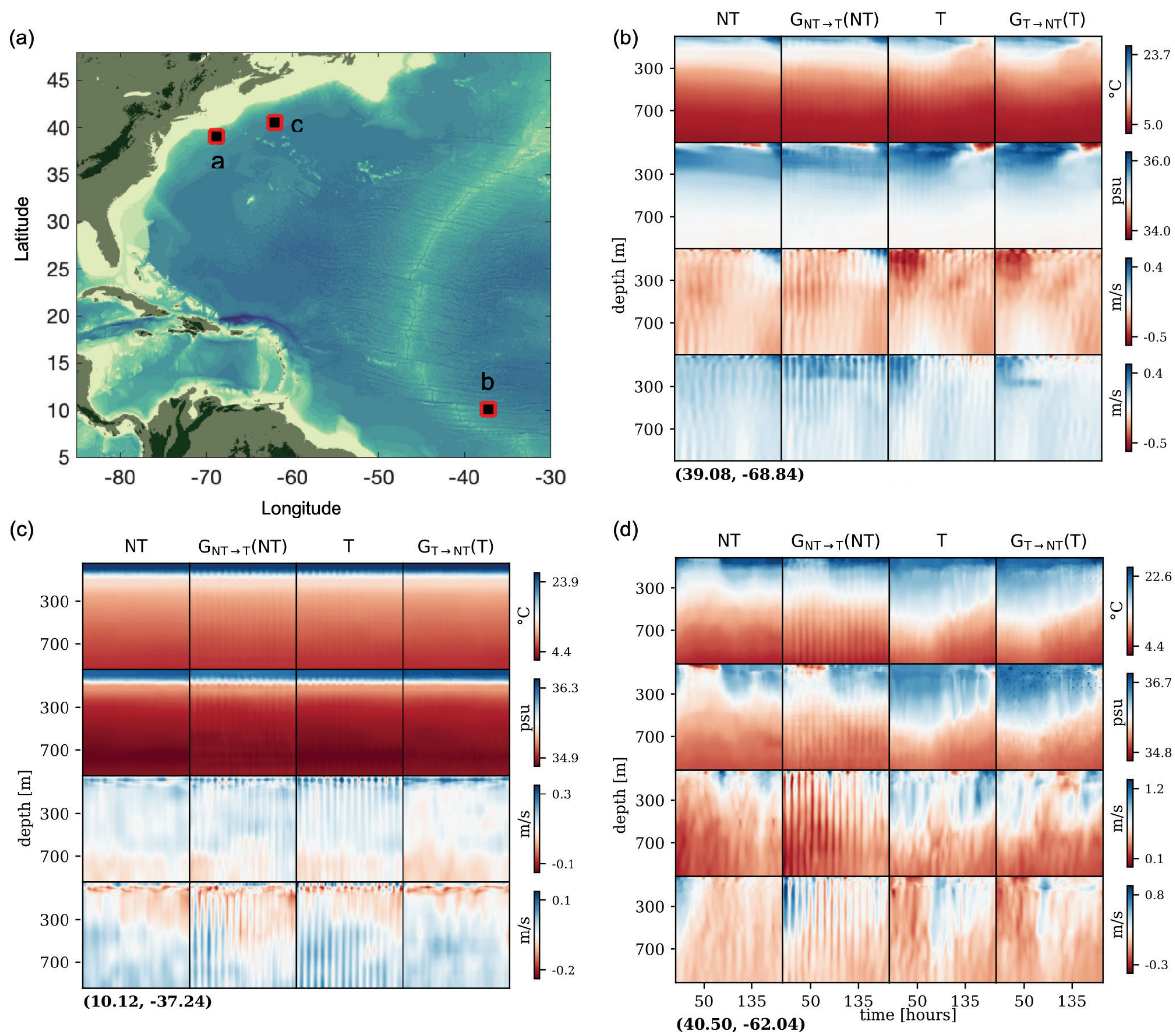

Figure 7. Temporal outputs of the trained DL model at the location noted in the bottom left of each subfigure (b)-(c), mapped in (a) For each panel: the first column is the non-tidal (NT) HYCOM results (Exp 19.2); the second column is the NT results translated into the tidal domain using the DL model; the third column is the tidal (T) HYCOM results (Exp 19.0); the fourth column is the T results translated into the NT domain using the DL model. Each row corresponds to the oceanographic variables from top to bottom: water temperature, salinity, eastward velocity, and northward velocity respectively.

References:

Alford, M. H., 2001. Internal Swell Generation: The Spatial Distribution of Energy Flux from the Wind to Mixed Layer Near-Inertial Motions. *Journal of Physical Oceanography,* 31, 2359–23, https://doi.org/10.1175/1520-0485(2001)031<2359:ISGTSD>2.0.CO;2

Alford, M. 2003. Redistribution of energy available for ocean mixing by long-range propagation of internal waves. *Nature* 423, 159–162. https://doi.org/10.1038/nature01628

Alford M.H., T. Peacock, J.A. MacKinnon, J.D. Nash, M.C. Buijsman, L.R. Centurioni, S.Y. Chao, M.H. Chang, D.M. Farmer, O.B. Fringer and others. 2015. The formation and fate of internal waves in the South China Sea. *Nature* 521(7550):65-9, https://doi.org/10.1038/nature14399

Ansong, J. K., B.K. Arbic, H.L. Simmons, M. H. Alford, M.C. Buijsman, P.G. Timko, A.J. Wallcraft. 2018. Geographical distribution of diurnal and semidiurnal parametric subharmonic instability in a global ocean circulation model. *Journal of Physical Oceanography* 48:1409-1431, https://doi.org/10.1175/JPO-D-17-0164.1

Arbic, B.K., S.T. Garner, R.W. Hallberg, H.L. Simmons. 2004. The accuracy of surface elevations in forward global barotropic and baroclinic tide models. *Deep-Sea Research II* 51:3069–3101, https://doi.org/10.1016/j.dsr2.2004.09.014

Arbic, B.K., A.J. Wallcraft, and E.J. Metzger. 2010. Concurrent simulation of the eddying general circulation and tides in a global ocean model. *Ocean Modelling*, 32, pp. 175-187, https://doi.org/10.1016/j.ocemod.2010.01.007

Arbic, B.K, J.G. Richman, J.F. Shriver, P.G. Timko, E.J. Metzger, and A.J. Wallcraft. 2012. Global modeling of internal tides within an eddying ocean general circulation model. *Oceanography*, 25, 20-29, https://doi.org/10.5670/oceanog.2012.38.

Arbic, B.K., M.H. Alford, J.K. Ansong, M.C. Buijsman, R.B. Ciotti, J.T. Farrar, R.W. Hallberg, C.E. Henze, C.N. Hill, C.A. Luecke and others. 2018. A primer on global internal tide and internal gravity wave continuum modeling in HYCOM and MITgcm. In *New frontiers in operational oceanography*, E. Chassignet, A. Pascual, J. Tintore, and J. Verron, Eds., GODAE OceanView, 307-392, https://doi.org/10.17125/gov2018.ch13.

Arbic, B.K. 2022. Incorporating tides and internal gravity waves within global ocean general circulation models: A review. *Progress in Oceanography* 206:102824, https://doi.org/10.1016/j.pocean.2022.102824.

Arbic, B.K., S. Elipot, J.M. Brasch, D. Menemenlis, A.L. Ponte, J.F. Shriver, X. Yu, E.D. Zaron, M.H. Alford, M.C. Buijsman and others. 2022. Near-surface oceanic kinetic energy distributions from drifter observations and numerical models. *Journal of Geophysical Research: Oceans* 127: e2022JC018551, https://doi.org/10.1029/2022JC018551

Barkan, R., K.B. Winters, K. B., & J.C. McWilliams, J. C. 2017. Stimulated Imbalance and the Enhancement of Eddy Kinetic Energy Dissipation by Internal Waves. *Journal of Physical Oceanography,* 47(1), 181-198. https://doi.org/10.1175/JPO-D-16-0117.1

Bell Jr., T. H. 1975. Topographically generated internal waves in the open ocean, *Journal of Geophysical Research*, 80(3), 320–327, doi:10.1029/JC080i003p00320. Bui

Buijsman, M. C., Y. Kanarska, and J.C. McWilliams. 2010. On the generation and evolution of nonlinear internal waves in the South China Sea, *Journal of Geophysical Research* 115:C02012, https://doi.org/10.1029/2009JC005275

Buijsman, M., G.R. Stephenson, J.K. Ansong, B.K. Arbic, M. Green, J.G. Richman, J.F. Shriver, and others. 2020. On the interplay between horizontal resolution and wave drag and their effect on tidal baroclinic mode waves in realistic global ocean simulations. *Ocean Modelling* 152:101656, https://doi.org/10.1016/j.ocemod.2020.101656

Chandrayadula, T.K., S. Periyasamy, J. A. Colosi, P.F. Worcester, M.A. Dzieciuch, J.A. Mercer, R.K. Andrew. 2020. Observations of low-frequency, long-range acoustic propagation in the Philippine Sea and comparisons with mode transport theory. *Journal of the Acoustical Society of America*, 147 (2): 877–897. https://doi.org/10.1121/10.0000587

Chassignet, E. P., L. T. Smith, G. R. Halliwell, and R. Bleck. 2003. North Atlantic Simulations with the Hybrid Coordinate Ocean Model (HYCOM): Impact of the Vertical Coordinate Choice, Reference Pressure, and Thermobaricity. *Journal of physical oceanography* 33:2504–2526, https://doi.org/10.1175/1520-0485(2003)033<2504:NASWTH>2.0.CO;2

Chassignet, E.P., H.E. Hurlburt, E.J. Metzger, O.M. Smedstad, J.A. Cummings, G.R. Halliwell, R. Bleck, R. Baraille, A.J. Wallcraft, C. Lozano, H.L. Tolman, A. Srinivasan, S. Hankin, P. Cornillon, R. Weisberg, A. Barth, R. He, F. Werner, and J. Wilkin. 2009. US GODAE: Global ocean prediction with the HYbrid Coordinate Ocean Model (HYCOM). *Oceanography* 22(2):64–75, https://doi.org/10.5670/oceanog.2009.39

Chassignet, E. P., and X. Xu. 2017. Impact of horizontal resolution (1/12° to 1/50°) on Gulf Stream separation, penetration, and variability. *Journal of Physical Oceanography* 47:1999−2021, https://doi.org/10.1175/JPO-D-17-0031.1

Chassignet, E.P., X. Xu, A. Bozec, and T. Uchida. 2023. Impact of the New England seamount chain on Gulf Stream pathway and variability. J. Phys. Oceanogr., 53, 1871-1886, doi:10.1175/JPO-D-23-0008.1

Colosi, J. A., and S.M. Flatté. 1996. Mode coupling by internal waves for multimegameter acoustic propagation in the ocean. *Journal of the Acoustical Society of America,* 100(6), 3607–3620. https://doi.org/10.1121/1.417334

tt

Dematteis, G., K. Polzin, and Y. V. Lvov. 2022. On the origins of the oceanic ultraviolet catastrophe. *Journal of Physical Oceanography* 52(4):597–616, https://doi.org/10.1175/JPO-D-21-0121.1

Dufau, C., M. Orsztynowicz, G. Dibarboure, R. Morrow, P.-Y. Le Traon. 2016. Mesoscale resolution capability of altimetry: Present and future. *Journal of Geophysical Research Oceans* 121:4910–4927, https://doi.org/10.1002/2015JC010904

Dushaw, B.D., B.D. Cornuelle, P.F. Worcester, B.M Howe, and D.S. Luther. 1995. Barotropic and baroclinic tides in the central North Pacific Ocean determined from long-range reciprocal acoustic transmission. *Journal of Physical Oceanography*. 25(4): 631–647. DOI: https://doi. org/10.1175/1520-0485(1995)025<0631:BABTIT> 2.0.CO;2

Dushaw, B.D., P.F. Worcester, M.A. Dzieciuch. 2011. On the predictability of mode-1 internal tides, *Deep Sea Research Part I: Oceanographic Research Papers,* 58(6):677-698, https://doi.org/10.1016/j.dsr.2011.04.002

Dushaw, B. D., and D. Menemenlis. 2023. Resonant diurnal internal tides in the North Atlantic: 2. Modeling. *Geophysical Research Letters*, 50, e2022GL101193. https://doi.org/10.1029/2022GL101193

Dzieciuch, M., W. Munk, D.L. Rudnick. 2004. Propagation of sound through a spicy ocean, the SOFAR overture. *Journal of the Acoustical Society of America.* 116 (3): 1447–1462. https://doi.org/10.1121/1.1772397

Eden, C., F. Pollmann, and D. Olbers. 2020. Towards a Global Spectral Energy Budget for Internal Gravity Waves in the Ocean, *Journal of Physical Oceanography* 50(4):935-944, https://doi.org/10.1175/JPO-D-19-0022.1

Egbert, G.D., A.F. Bennett and M.G.G Foreman. 1994. Topex/Poseidon tides estimated using a global inverse model. *Journal of Geophysical Research* 99:24821–24852, https://doi.org/10.1029/94JC01894.

Flatté, S. M., R. Dashen, W. Munk, K. Watson, K., and F. Zachariasen, F. 1979. *Sound Transmission Through a Fluctuating Ocean.* Cambridge Univeristy Press. Cambridge.

Garrett, C., and E. Kunze, 2007. Internal Tide Generation in the Deep Ocean. *Annual Review of Fluid Mechanics* 39(1):57-87. https://doi.org/10.1146/annurev.fluid.39.050905.110227

Garrett, C., and Munk, W. 1975. Space-time scales of internal waves: A progress report, *Journal of Geophysical Research*, 80(3), 291–297, https://doi.org/10.1029/JC080i003p00291

Garrett, C., and W. Munk. 1979. Internal waves in the ocean. *Annual Review of Fluid Mechanics*, 11(1):339–369, https://doi.org/10.1146/annurev.fl.11.010179.002011.

Gill, Adrian E. 1982. *Atmosphere-ocean dynamics.* Vol. 30. Academic press, London, UK, 1982.

Goodfellow, I. J., J. Pouget-Abadie, M. Mirza, B. Xu, D. Warde-Farley, S. Ozair, A. Courville, and Y Bengio. 2014. Generative Adversarial Networks. *ArXiv:1406.2661 [Cs, Stat]*. http://arxiv.org/abs/1406.2661

Goodfellow, I., Bengio, Y., & Courville, A. (2016). *Deep Learning*. MIT Press. http://www.deeplearningbook.org

Helber, R. W., C.N. Barron, M.R. Carnes and R.A. Zingarelli. 2008. Evaluating the sonic layer depth relative to the mixed layer depth. *Journal of Geophysical Research* 113:C07033. https://doi.org/10.1029/2007JC004595

Hendershott, M.C. (1981) Long waves and ocean tides. B. Warren, C. Wunsch (Eds.), Evolution of Physical Oceanography, MIT Press (1981), pp. 292-341

Hiron, L., P. Miron, L.K. Shay, W.E. Johns, E.P. Chassignet, and A. Bozec, 2022: Lagrangian Coherence and Source of Water of Loop Current Frontal Eddies in the Gulf of Mexico. *Progress in Oceanography*. pp. 102876, ISSN 0079-6611. https://doi.org/10.1016/j.pocean.2022.102876.

Hiron, L., D.S. Nolan, and L.K. Shay, 2021: Study of Ageostrophy during Strong, Nonlinear Eddy-Front Interaction in the Gulf of Mexico, *Journal of Physical Oceanography*, 51(3), 745-755. https://doi.org/10.1175/JPO-D-20-0182.1.

Hogan, T.F., M. Liu, J.A. Ridout, M.S. Peng, T.R. Whitcomb, B.C. Ruston, C.A. Reynolds, S.D. Eckermann, J.R. Moskaitis, N.L. Baker, J.P. McCormack, K.C. Viner, J.G. McLay, M.K. Flatau, L. Xu, C. Chen, and S.W. Chang. 2014. The Navy Global Environmental Model. *Oceanography* 27(3):116–125, https://doi.org/10.5670/oceanog.2014.73

Kelly, S. M., A. F. Waterhouse, and A. C. Savage. 2021. Global dynamics of the stationary M2 Mode-1 internal tide. *Geophysical Research Letters* 48:e2020GL091692, https://doi.org/10.1029/2020GL091692

Lamb, K. G. 2004. Nonlinear interaction among internal wave beams generated by tidal flow over supercritical topography, *Geophysical Research Letters* 31:L09313, https://doi.org/1029/2003GL019393.

Luecke, C.A., B.K. Arbic, J.G. Richman, J.F. Shriver, M.H. Alford, J.K. Ansong, S.L. Bassette, M.C. Buijsman, D. Menemenlis, R.B. Scott, and others. 2020. Statistical comparisons of temperature variance and kinetic energy in global ocean models and observations: Results from mesoscale to internal wave frequencies. *Journal of Geophysical Research: Oceans* 125:e2019JC015306, https://doi.org/10.1029/2019JC015306.

MacKinnon, J. A., Z. Zhao, C.B. Whalen, A.F. Waterhouse, D.S. Trossman, O.M. Sun, L.C. St. Laurent, H.L. Simmons, K. Polzin, R. Pinkel, A. Pickering, N.J. Norton, J.D. Nash, R. Musgrave, L.M. Merchant, A.V. Melet, B. Mater, S. Legg, W.G. Large, E. Kunze, J. Klymak, M. Jochum, S.R. Jayne, R.W. Hallberg, S.M. Griffies, S. Diggs, G. Danabasoglu, E.P. Chassignet, M.C. Buijsman, F.O. Bryan, B.P. Briegleb, A. Barna, B.K. Arbic, J.K. Ansong, and M.H. Alford.

2017. Climate Process Team on Internal Wave–Driven Ocean Mixing. *Bulletin of the American Meteorological Society*, 98(11), 2429-2454. https://doi.org/10.1175/BAMS-D-16-0030.1

Marshall, J., A. Adcroft, C. Hill, L. Perelman, C. Heisey. 1997. A finite-volume, incompressible Navier Stokes model for studies of the ocean on parallel computers. *Journal of Geophysical Research* 102:5753–5766, https://doi.org/10.1029/96JC02775.

Metzger, E.J., O.M. Smedstad, P.G. Thoppil, H.E. Hurlburt, J.A. Cummings, A.J. Wallcraft, L. Zamudio, D.S. Franklin, P.G. Posey, M.W. Phelps, P.J. Hogan, F.L. Bub, and C.J. DeHaan. 2014. US Navy operational global ocean and Arctic ice prediction systems. *Oceanography* 27(3):32–43, http://doi.org/10.5670/oceanog.2014.66

McComas, C. H., and F. P. Bretherton. 1977. Resonant interaction of oceanic internal waves. *Journal of Geophysical Research* 82(9):1397–1412, https://doi.org/10.1029/JC082i009p01397.

Müller, M., B.K. Arbic, J.G. Richman, J. F. Shriver, E.L. Kunze, R.B. Scott, A.J. Wallcraft, and L. Zamudio, L. 2015. Toward an internal gravity wave spectrum in global ocean models. *Geophysical Research Letters*, 42, 3474–3481. https://doi.org/10.1002/2015GL063365

Müller, P., G. Holloway, F. Henyey, F., and N.Pomphrey, N. 1986. Nonlinear interactions among internal gravity waves, *Reviews of Geophysics*, 24(3), 493–536, https://doi.org/10.1029/RG024i003p00493

Munk, W. H., and C. Wunsch, 1998. Abyssal recipes II: Energetics of tidal and wind mixing. *Deep-Sea Research I,* 45, 1977–2010, https://doi.org/10.1016/S0967-0637(98)00070-3.

Nelson, A., B. Arbic, D. Menemenlis, W. Peltier, M. Alford, N. Grisouard, and J. Klymak. 2020. Improved internal wave spectral continuum in a regional ocean model. *Journal of Geophysical Research: Oceans* 125(5), https://doi.org/10.1029/2019JC015974.

Ngodock, H. E., I. Souopgui, A. J. Wallcraft, J. G. Richman, J. F. Shriver, and B. K. Arbic. 2016. On improving the accuracy of the barotropic tides embedded in a high-resolution global ocean circulation model. *Ocean Modelling* 97:16-26, https://doi.org/10.1016/j.ocemod.2015.10.011

Olbers DJ. 1976. Nonlinear energy transfer and the energy balance of the internal wave field in the deep ocean. Journal of Fluid Mechanics. 74(2):375-399. https://doi.org/10.1017/S0022112076001857

Pan, Y., B.K. Arbic, A.D. Nelson, D. Menemenlis, W.R. Peltier, W. Xu, and Y Li. 2020. Numerical investigation of mechanisms underlying oceanic internal gravity wave power-law spectra. *Journal of Physical Oceanography* 50:2713–2733. https://doi.org/10.1175/JPO-D-20-0039.1

Porter, Michael. 2011. The BELLHOP Manual and User's Guide: PRELIMINARY DRAFT. http://oalib.hlsresearch.com/Rays/HLS-2010-1.pdf. Accessed 23 March 2023.

Raja, K. J., M.C. Buijsman, J.F. Shriver, B.K. Arbic and O. Siyanbola. 2022. Near-inertial wave energetics modulated by background flows in a global model simulation. *Journal of Physical Oceanography* 52(5):823-840, https://doi.org/10.1175/JPO-D-21-0130.1

Raja, K.J., M.C. Buijsman, A. Bozec, R.W. Helber, J.F. Shriver, A. Wallcraft, E.P. Chassignet, and B.K. Arbic.2024. Spurious internal wave generation during data assimilation in eddy resolving ocean model simulations. Ocean Modelling, 188, p.102340, https://doi.org/10.1016/j.ocemod.2024.102340

Rudnick, D. 2016. California Underwater Glider Network [Data set]. Scripps Institution of Oceanography, Instrument Development Group. https://doi.org/10.21238/S8SPRAY1618

Shriver, J. F., B.K. Arbic, J.G. Richman, R.D. Ray, E.J. Metzger, A.J. Wallcraft, and P.G. Timko. 2012. An evaluation of the barotropic and internal tides in a high-resolution global ocean circulation model. Journal of Geophysical Research. 117, C10024, https://doi.org/10.1029/2012JC008170

Simmons, H.L., R.W. Hallberg, and B.K. Arbic. 2004. Internal wave generation in a global baroclinic tide model. *Deep-Sea Research II*, 51:3043–3068. https://doi.org/10.1016/j.dsr2.2004.09.015

Simmons, H.L., and M.H. Alford. 2012. Simulating the long-range swell of internal waves generated by ocean storms. *Oceanography* 25(2):30–41, https://doi.org/10.5670/oceanog.2012.39.

Skitka, J., B.K. Arbic, R. Thakur, D. Menemenlis, W.R. Peltier, Y. Pan, K. Momeni, and Y Ma. 2024. Probing the nonlinear interactions of supertidal internal waves using a high-resolution regional ocean model. In press for *Journal of Physical Oceanography*, https://doi.org/10.1175/JPO-D-22-0236.1

Solano, M., M.C. Buijsman, J.F. Shrive, J. Magalhaes, J.C. Da Silva, C. Jackson, B.K. Arbic, and R. Barkan. 2023. Nonlinear internal tides in a realistically forced global ocean simulation. *Journal of Geophysical Research,* 128, e2023JC019913, https://doi.org/10.1029/2023JC019913

Stewart, K.D., A.M.C. Hogg, S.M. Griffies, A.P. Heerdegen, M.L. Ward, P. Spence, and M.H. England. 2017. Vertical resolution of baroclinic modes in global ocean models. *Ocean Modelling* 113:50–65, https://doi.org/10.1016/j.ocemod.2017.03.012

Thakur, R., B.K. Arbic, D. Menemenlis, K. Momeni, Y. Pan, W.R. Peltier, J. Skitka, M.H. Alford, and Y. Ma, 2022: Impact of vertical mixing parameterizations on internal gravity wave spectra in regional ocean models. *Geophysical Research Letters* 49:e2022GL099614, https://doi.org/10.1029/2022GL099614

Waterhouse, A. F., and Coauthors, 2014: Global Patterns of Diapycnal Mixing from Measurements of the Turbulent Dissipation Rate. *Journal of Physical Oceanography*, 44, 1854–1872, https://doi.org/10.1175/JPO-D-13-0104.1.

Xu, X., E.P. Chassignet, A.J. Wallcraft, B.K. Arbic, M.C. Buijsman and M. Solano. 2022. On the spatial variability of the mesoscale sea surface height wavenumber spectra in the Atlantic Ocean. *Journal of Geophysical Research: Oceans* 127:e2022JC018769, https://doi.org/10.1029/2022JC018769

Xu, Y., and L.-L. Fu. 2012. The effects of altimeter instrument noise on the estimation of the wavenumber spectrum of sea surface height. *Journal of Physical Oceanography* 42:2229–2233, https://doi.org/10.1175/JPO-D-12-0106.1

Worcester, P. F., M. A.Dzieciuch, J.A., Mercer, R.K. Andrew, B.D. Dushaw, A.B. Baggeroer, K.D. Heaney, G.L. D'Spain, J.A. Colosi, R.A. Stephen, J.N. Kemp, B.M Howe, L/J/Van Uffelen, and K.E. Wage (2013). The North Pacific Acoustic Laboratory deep-water acoustic propagation experiments in the Philippine Sea. *Journal of the Acoustical Society of America*, 134, 3359–3375. https://doi.org/10.1121/1.4818887

Zhou, X.-H., D.-P Wang, and D. Chen. 2015. Global wavenumber spectrum with corrections for altimeter high frequency noise. *Journal of Physical Oceanography* 45(2):495-503, https://doi.org/10.1175/JPO-D-14-0144.1.

Zhu, J. Y., T. Park, P. Isola, and A.A. Efros. 2017. Unpaired image-to-image translation using cycle-consistent adversarial networks. Pp. 2223-2232 in *Proceedings of the IEEE international conference on computer vision*. Venice, Italy. https://doi.org/10.1109/ICCV.2017.244